JOM
https://doi.org/10.1007/s11837-026-08266-w

TECHNICAL ARTICLE

Wear Behavior of TiB_2–C_3N_4 Composites Fabricated by SPS Process

MILAD SAKKAKI,[1] SEYED MOHAMMAD ARAB,[2,5] ZOHRE AHMADI,[3,6] MOHAMMAD FARVIZI,[4] and MEHDI SHAHEDI ASL[3,7]

1.—Department of Mechanical Engineering, Faculty of Manufacturing, University of Tabriz, Tabriz 51666-16471, Iran. 2.—Department of Materials and Manufacturing Engineering, University of Mohaghegh Ardabili, Ardabil 56199-11367, Iran. 3.—Department of Mechanical Engineering, Faculty of Engineering, University of Kyrenia, Kyrenia, Mersin 10, Turkey. 4.—Department of Materials Engineering, Faculty of Mechanical Engineering, University of Tabriz, Tabriz 51666-16471, Iran. 5.—e-mail: m.arab@uma.ac.ir. 6.—e-mail: zohre.ahmadi@kyrenia.edu.tr. 7.—e-mail: mehdi.shahediasl@kyrenia.edu.tr

Ultra-high-temperature ceramics (UHTCs), particularly titanium diboride (TiB_2), are critical for demanding applications such as thermal protection systems, wear-resistant components, and high-temperature applications. However, their strong covalent bonding and poor sinterability pose significant fabrication challenges. This study investigates the incorporation of graphitic carbon nitride (g-C_3N_4) as a sintering aid and reinforcing phase in TiB_2 composites processed via spark plasma sintering (SPS). A TiB_2-10 wt% g-C_3N_4 composite was sintered at 1900°C under a pressure of 40 MPa, achieving a relative density of 91.3%. Tribological evaluation via pin-on-disk testing revealed a specific wear rate of 2.455×10^{-4} mm^3/N m, approximately half that of monolithic TiB_2, alongside an estimated hardness of 41.2 GPa. Microstructural analysis identified carbon-rich tribofilms and probably in- situ formed B_4C nanoparticles as key contributors to enhanced wear resistance. However, the composite exhibited a higher average coefficient of friction (0.67) compared to pure TiB_2, attributed to less effective lubrication from the tribofilm. These findings demonstrate g-C_3N_4 as a promising additive for improving the wear performance of TiB_2-based composites while highlighting the need for further optimization to reduce frictional losses.

INTRODUCTION

With the rapid advancement of technology and industrial development, there is a growing demand for materials with novel and tailored properties. These materials are critical for specialized applications, including high-temperature environments such as hypersonic vehicle thermal protection systems (TPS), turbine engines, and combustion chambers. Additionally, they are essential for heavy-wear conditions and high-temperature mechanical performance. Furthermore, their utility extends to biomedical applications and refractory uses, where exceptional durability and stability are required.[1–3]

To address these challenges, researchers have developed a class of advanced materials called ultra-high-temperature ceramics (UHTCs). These ceramics exhibit exceptional properties, including an extremely high melting point, superior thermal conductivity, outstanding thermal stability, and remarkable resistance to thermal shock, corrosion, and wear. Furthermore, they demonstrate excellent mechanical performance at elevated temperatures, characterized by high strength, an optimal strength-to-weight ratio, and excellent chemical compatibility.[4–6]

(Received December 2, 2025; accepted February 24, 2026)

Published online: 18 May 2026

Research on UHTCs can be broadly classified into two main categories. The first category encompasses experimental investigations, which examine the influence of various additives, processing parameters (such as temperature and pressure), and their effects on densification behavior, microstructural evolution, mechanical properties, and underlying strengthening mechanisms. The second category involves computational studies, focusing on numerical simulations of temperature and pressure distributions within samples and equipment, the role of geometric parameters, and energy optimization during UHTC manufacturing processes.[7–10]

The transition metal carbides, nitrides, and borides (particularly those containing Zr, Hf, Ta, Ti, and Nb) constitute the primary family of UHTCs.[11] Among these, metal borides with melting points exceeding 3000 °C, including TiB_2,[12] ZrB_2,[13] and HfB_2,[14,15] have garnered significant research interest due to their exceptional combination of properties. These include superior mechanical characteristics, outstanding chemical stability, and remarkable resistance to erosion and oxidation.[16] Among different metallic borides, titanium diboride that crystallizes in a hexagonal close-packed (HCP) structure,[4] exhibits an extraordinary combination of properties; a relatively low density (4.52 g/cm^3), an ultra-high melting temperature (3225 °C), extreme hardness (22–25 GPa, approximately three times greater than that of fully hardened steel), a high elastic modulus (500 GPa), excellent chemical inertness, and exceptional oxidation resistance (with oxide phases remaining stable above 2700 °C). Furthermore, TiB_2 demonstrates advantageous thermal characteristics, including a low coefficient of thermal expansion coupled with substantial thermal and electrical conductivity.[17–19] This unique property profile establishes TiB_2 as an outstanding candidate material for numerous advanced technological applications. These include TPS, impact-resistant armor components, wear-resistant mechanical parts, high-performance cutting tools, and specialized electrodes for high-temperature metal refining processes.[20]

Despite these advantages, the fabrication of phase-pure UHTCs (including monolithic TiB_2) faces significant challenges due to their strong covalent bonding, low sinterability, and limited self-diffusion coefficients.[21] To address these limitations, researchers have developed several processing strategies. One approach involves simultaneous high-temperature and high-pressure sintering to achieve fully dense TiB_2. However, this method presents inherent limitations, as the required high sintering temperatures often promote excessive grain growth, ultimately degrading the mechanical properties.[22–24]

An alternative and more widely studied technique incorporates additives as secondary phases. Extensive research has demonstrated that various additives can serve dual roles as both sintering aids and reinforcing phases in TiB_2-based composites, significantly improving densification and mechanical performance.[25] These additives can be categorized into several classes: carbon-based materials such as carbon nanotubes, graphene nanoplatelets (GNPs), carbon fibers, intermetallics such as NiCr, ceramic compounds such as Al_2O_3, B_4C, SiC, TiC, nitrides, such as AlN, BN, Si_3N_4, HfN, TiN, disilicides, such as WSi_2, $MoSi_2$, $TiSi_2$, and CrSi, and metallic elements such as Ti, Ta, Ni, Fe, Al, Cr, Mo, Co, and Cu. Recently, carbon nitride (C_3N_4) has emerged as a proper additive. While traditionally employed for catalytic applications,[26] C_3N_4 has found new utility in materials engineering as sintering aid and reinforcement phase in composites[27], as well as a coating material for cutting tools.[28,29] These additives function through multiple mechanisms, removing surface oxide layers from powder particles or forming new in situ phases during processing, thereby enhancing both sinterability and mechanical properties.[30–32] TiB_2-based composites are also densified by several methods, including pressureless sintering, hot pressing, hot isostatic pressing, reactive hot pressing, laser-assisted sintering, microwave sintering, and spark plasma sintering (SPS).

The various sintering methods differ primarily in their heat generation mechanisms and pressure application techniques. Among them, SPS represents a relatively novel and rapid consolidation method that uniquely combines uniaxial pressure with a pulsed direct current. This simultaneous application enables exceptional heating rates while maintaining comparatively low bulk sintering temperatures, significantly improving the densification of traditionally difficult-to-sinter ceramic materials.[33,34] In the SPS process, powder materials are loaded into a conductive die positioned between two punch electrodes. The system then applies both mechanical pressure (typically ranging from 30 MPa to 100 MPa) and a high-amperage pulsed current. This combination generates microscopic electric discharges at particle contacts, creating localized plasma and intense Joule heating effects. These phenomena facilitate rapid particle surface activation and enhance atomic diffusion, ultimately leading to accelerated densification kinetics while minimizing undesirable grain growth.[35,36]

Wear resistance represents a critical mechanical property for structural applications, particularly in TiB_2-based composites where additives play a key role in determining tribological performance. Extensive research has demonstrated that the incorporation of various additives significantly influences wear characteristics through multiple mechanisms. The selection and optimization of sintering additives, including their type and concentration, have been shown to substantially enhance both mechanical properties and wear resistance in these composite systems.[37] Studies consistently highlight that proper additive formulation can improve key wear-

related properties such as surface hardness, fracture toughness, and interfacial bonding strength, all of which contribute to superior wear performance under operational conditions.

The addition of Si_3N_4 into TiB_2-based composites promotes the formation of beneficial in situ phases during sintering, achieving high relative densities of 98.8–99.5%. However, the addition of B_4N to the TiB_2–Si_3N_4 system reduces both density and hardness. Interestingly, the hardness of TiB_2-Si_3N_4-B_4N composites correlates directly with densification levels while exhibiting an inverse relationship with fracture toughness. The optimal composition of TiB_2 + 30% Si_3N_4 + 3% B_4N demonstrates exceptional wear resistance, combining densification (99.5%) with balanced mechanical properties, including a hardness of 25.2 GPa.[37]

Silicon carbide (SiC) has emerged as a particularly effective additive for TiB_2-based composites. When incorporated via SPS, the addition of 10–20 wt% SiC to TiB_2 composites leads to three key improvements: (1) enhanced microstructural refinement, (2) increased densification (achieving up to 99.5% theoretical density), and (3) superior mechanical properties including a maximum hardness of 25.5 GPa. Tribological studies demonstrate that higher SiC content progressively improves wear performance through multiple mechanisms: reduction in the coefficient of friction, decreased wear rate, and consequently enhanced wear resistance.[38]

The role of GNPs in TiB_2-SiC composites sintered via field-assisted techniques at 2100°C under an argon atmosphere was investigated. The results demonstrated that GNP incorporation produces competing effects, while enhancing fracture toughness and flexural strength, simultaneously reducing composite hardness. Notably, increasing GNP content significantly improves wear resistance through the formation of protective SiO_2-TiO_2-C tribochemical layers on contact surfaces.[39,40]

Building on innovative additive research, Ahmadi et al.[27] pioneered the application of graphitic carbon nitride (g-C_3N_4) as both a sintering aid and reinforcement in ZrB_2 matrices processed by SPS. Their work revealed that 5 wt% g-C_3N_4 addition dramatically improved sinterability, elevating relative density from 76.5% to 99.8% while enhancing mechanical properties. Motivated by these results, the current study explores g-C_3N_4 as a cost-effective additive for TiB_2 composites, specifically targeting wear performance improvement. A monolithic TiB_2 and a TiB_2-g-C_3N_4 composite were produced using the SPS method to assess the effectiveness of g-C_3N_4 as an additive, its possible role as a reinforcing phase, and the resulting enhancements in tribological properties.

EXPERIMENTAL

Material Preparation

The matrix material consisted of commercial TiB_2 powder (Xuzhou Hongwu) with a particle size distribution of 3–8 μm and 99.9% purity. The reinforcing phase, g-C_3N_4 powder (> 99% purity), was synthesized from melamine precursors. A TiB_2–10 wt% g-C_3N_4 composite was prepared through the following steps:

- **Weighing and Mixing**: Precise quantities of TiB_2 and g-C_3N_4 powders were measured using an analytical balance and dispersed in ethanol.
- **Ultrasonic Homogenization**: The suspension underwent 30 min of ultrasonic treatment to ensure uniform particle distribution.
- **Solvent Removal:**
- **Primary drying**: Magnetic stirring to achieve a semi-dry state
- **Secondary drying**: Oven treatment at 120 °C for 12 h for complete ethanol evaporation
- **Powder Processing**: The dried mixture was de-agglomerated and sieved through a 100-mesh screen (149-μm openings) to obtain a homogeneous precursor powder.

TiB_2-g-C_3N_4 (TC) Composite Fabrication

The SPS method was used to fabricate the samples. The sintering process was carried out using an SPS-20T-10 furnace. Temporal, thermal, displacement, and current data were measured continuously throughout the process. A water-circulating cooling system was included in the device to prevent excessive heating of the machine components and the vacuum chamber. To reduce heat dissipation from the chamber, the mold's surfaces were coated with fireproof felt. To inhibit chemical interactions between the powder mixture and the graphite die, graphite foil was strategically placed across the inner section of the die. To facilitate sample removal, the graphite foil was positioned at the interface between the punch and the sample. The samples underwent sintering for 7 min at 1900°C with a pressure of 40 MPa. Following the sintering process, the sintered samples were extracted using a hydraulic press, and the graphite foil stuck to the surface was removed by grinding. To prepare for microstructural examinations, the samples' surfaces were polished with suitable sandpapers.

The schematic of the experimental procedure, as explained "Material Preparation" and "TiB_2-g-C_3N_4 (TC) Composite Fabrication" sections, is shown in Fig. 1.

Characterization

The relative density of the sintered samples was calculated using a densitometer based on Archimedes' principle, with distilled water as the immersion medium. Utilizing a Philips PW1730 machine and the X'Pert HighScore Plus software, phase analysis of materials was conducted using the XRD method. The microstructure analysis of the samples

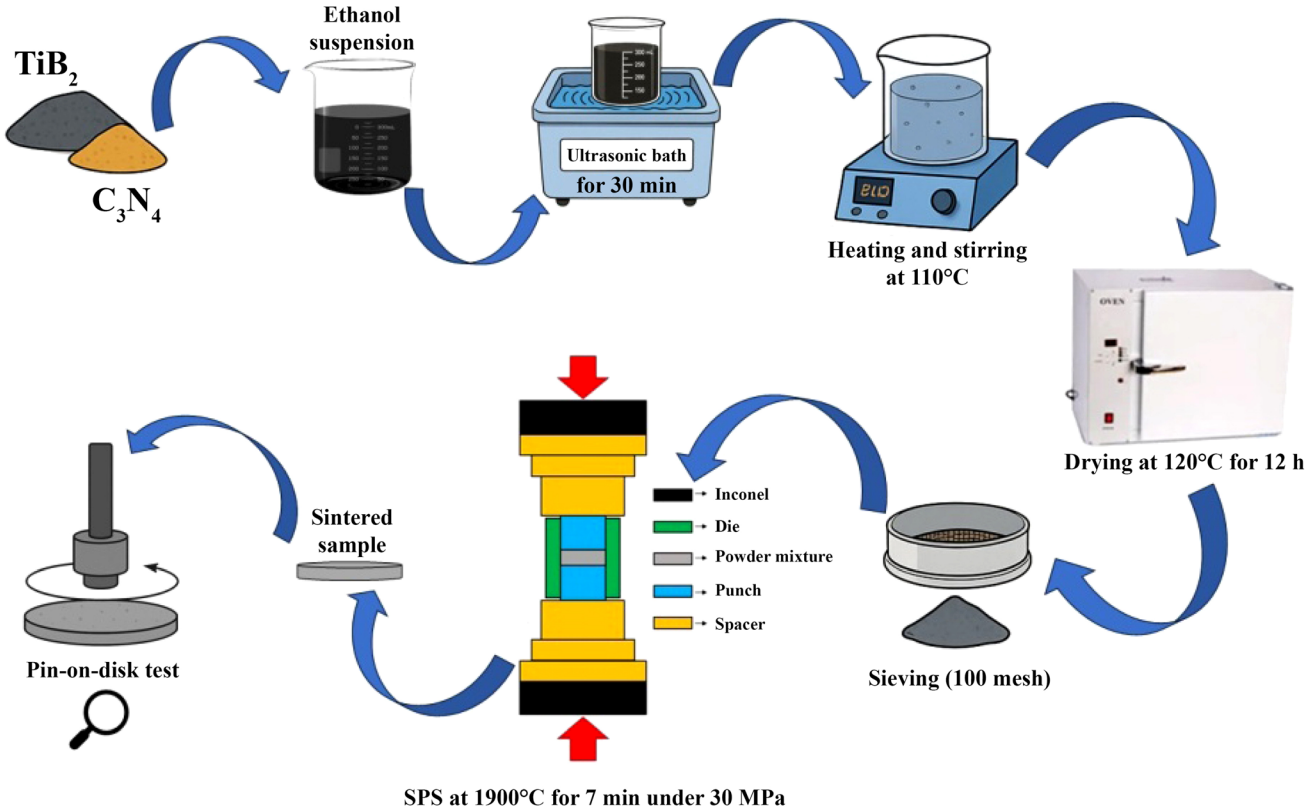

Fig. 1. Schematic of experimental procedure in the current study.

was investigated with a field-emission scanning electron microscope (FESEM; Mira3; Tescan). EDS analysis was applied to determine the chemical composition of the selected points in the samples' microstructure. In this research, the pin-on-disc method has been used to investigate the friction and wear behavior of the prepared composite. The wear test was carried out in accordance with the standard ASTM G99-05 (2016). In this test, the pin is tungsten carbide (WC) with a diameter of 5 mm. Additionally, the sensors embedded in the recording device automatically determined the composite's friction coefficient. After the wear test, the samples' surfaces were examined by a scanning electron microscope (SEM). After measuring the average width of the worn area according to the device's specifications and test conditions, the wear rate was calculated using Eqs. 1 and 2:

The characterization of the samples was carried out through the following steps and devices.

- **Density Measurement:**

– Relative density was determined via Archimedes' principle using a precision densitometer.
– Distilled water served as the immersion medium (ρ = 0.998 g/cm^3 at 20°C).
– Measurements were repeated three times to ensure statistical reliability.

- **Phase Analysis:**

– XRD characterization performed using a Philips PW1730 diffractometer.
– Configuration: Cu Kα radiation (λ = 1.5406 Å), 40 kV, 30 mA.
– Data processed with X'Pert HighScore Plus software (PANalytical).
– Scanning range (2θ): 10–90° with 0.02° step size.

- **Microstructural Characterization:**

– EFSEM operated at 20 kV.
– Secondary electron (SE) and backscattered electron (BSE) imaging modes.
– EDS analysis for elemental composition (spot size: 1 μm, acquisition time: 60 s).

- **Tribological Evaluation:**

– Pin-on-disk testing per ASTM G99-05 (2016) standard.
– Test parameters:

– Counterface: WC pin (Ø 5 mm, hardness 1600 HV).
– Normal load: 30 N.
– Testing angular speed: 20 rpm.
– Pin path radius: 10 mm.
– Sliding speed: 0.08 m/s.
– Sliding distance: 100 m.
– Ambient conditions: 25°C, 40% humidity.

- In situ friction coefficient monitoring via integrated sensors.
- Post-test analysis:
- FESEM examination of wear tracks.
- Specific wear rate calculation via:

$$V = \frac{\pi R d^3}{6r} \quad (1)$$

$$\text{specific wear rate} = \frac{V}{N \times S} \quad (2)$$

where R (mm) is the distance from center of the wear line to center of the sample, d (mm) is the average width of worn area, r (mm) is the pin tip radius, V (mm^3) is the volume of lost wear area, S (m) is the total sliding length, and N (N) is the normal force.

RESULTS AND DISCUSSION

Comparing the theoretical density of TiB_2 (4.52 g/cm^3) and TiB_2-10 wt% g-C_3N_4 (4.17 g/cm^3), the composite achieved a relative density of 91.3%. The relative density of monolithic TiB_2 was 96.7%. The XRD patterns (Fig. 2) indicated the following observations.

1. In situ generation of hexagonal-BN and probably other hard allotropes of BN occurred through a reaction cascade. The cubic-BN and orthorhombic-BN peaks in XRD may overlap with strong TiB_2 peaks or the amount of the newly formed phases may be so small that they cannot be detected by means of XRD examination. The enhancement of mechanical properties specifies that some of these hard phases have contributed to significant improvement in mechanical strength and tribological performance.
2. The potential formation of B_4C in situ phases cannot be ruled out, though their detection threshold likely falls below the XRD detection limits owing to trace-level concentrations.

The comprehensive analysis of XRD test results is available in prior research.[42] Figure 3 illustrates the FE-SEM micrograph of the TC sample. The light-gray zones are TiB_2 particles. The dark-colored phases may correspond to BN allotropes and carbon, as the g-C_3N_4 particles decompose into their constituent elements at high temperatures. Detailed examinations of EDS analysis in the previous work[42] also confirm the formation of in situ phases.

Figure 4 represents FE-SEM micrographs illustrating the wear tracks generated by the tungsten carbide (WC) pin on the TiB_2-g-C_3N_4 composite surface. In order to quantitative wear analysis, the wear track width was measured at several locations and averaged to calculate the wear volume and wear rate.

The surface loses its mechanical integrity, generating debris that detaches from the contact zone. Unlike Young's modulus, which is an intrinsic material property, wear depends on the tribosystem parameters, including speed, time, temperature, and applied force.[34] The SE mode in FFESEM Microscopy provides high-resolution surface topography, whereas the BSE mode generates compositional contrast based on atomic number. After measurements at several points, the average width of the wear track was determined to be 703 μm. Using the experimental data provided in Section 3-2 and Eqs. 1 and 2, the average volume loss along the track was calculated as 0.7276 mm^3, and the volumetric specific wear rate was found to be 2.455×10^{-4} mm^3/N m which is around half of monolithic TiB_2 ($\sim 5 \times 10^{-4}$ mm^3/N m).[38]

The improvement in wear resistance can be attributed to the efficient protection of hard particles, such as probable hard allotropes of BN and B_4C, on the TiB_2 matrix, which limit both fracture and plastic deformation in the composite. The hexagonal BN could also decrease the wear rate due to its lubricating nature. According to Archard's law, the wear rate of a material is inversely proportional to its hardness. In addition to the nature and extremely high hardness of TiB_2, and since the use of in situ phases as a reinforcing phase increased the relative density, the porosity of the composite also decreased, leading to an enhancement in the sample's hardness, which is because the pores in the sample offer no resistance to indentation penetration, consequently achieving a dense material resulting in higher hardness, which leads to a reduction in wear rate.[43]

Directional scratches indicate relative motion between surfaces in a specific direction. Local variations in roughness may result from porosity, fatigue cracks, or separation of hard/soft phases in the composite. Irregular pits and grooves (Fig. 4a, white arrows) showed that the hard particles (Fig. 4b, white circles) have been dragged across the surface. There is also no evidence of adhesive wear such as plastic deformation or welded protrusions. The micro-pores (Fig. 4a, white squares) can act as stress concentrators, accelerating wear.

Figure 5 represents the FESEM micrograph of the worn surface of the TiB_2-g-C_3N_4 composite at higher magnification. As indicated in Fig. 5a, microcracks are observable on the worn surface, confirming the fatigue wear mechanism in this sample.[44] The brighter debris on the surface, which is visible in the BS image (Fig. 5b), can be caused by surface contaminants, wear products, brittle particles, or wear of the abrasive pin.

Since carbon nitride was used as an additive in this study, severe carbon accumulation in certain regions is observed (Fig. 6). The carbon-rich areas, along with the matrix and pin, gradually wear down into fine particles, which either fill the grooves formed by abrasion or act as a lubricating film, thereby significantly reducing wear intensity. This mechanism can be considered as one of the factors contributing to the decreased volumetric wear rate

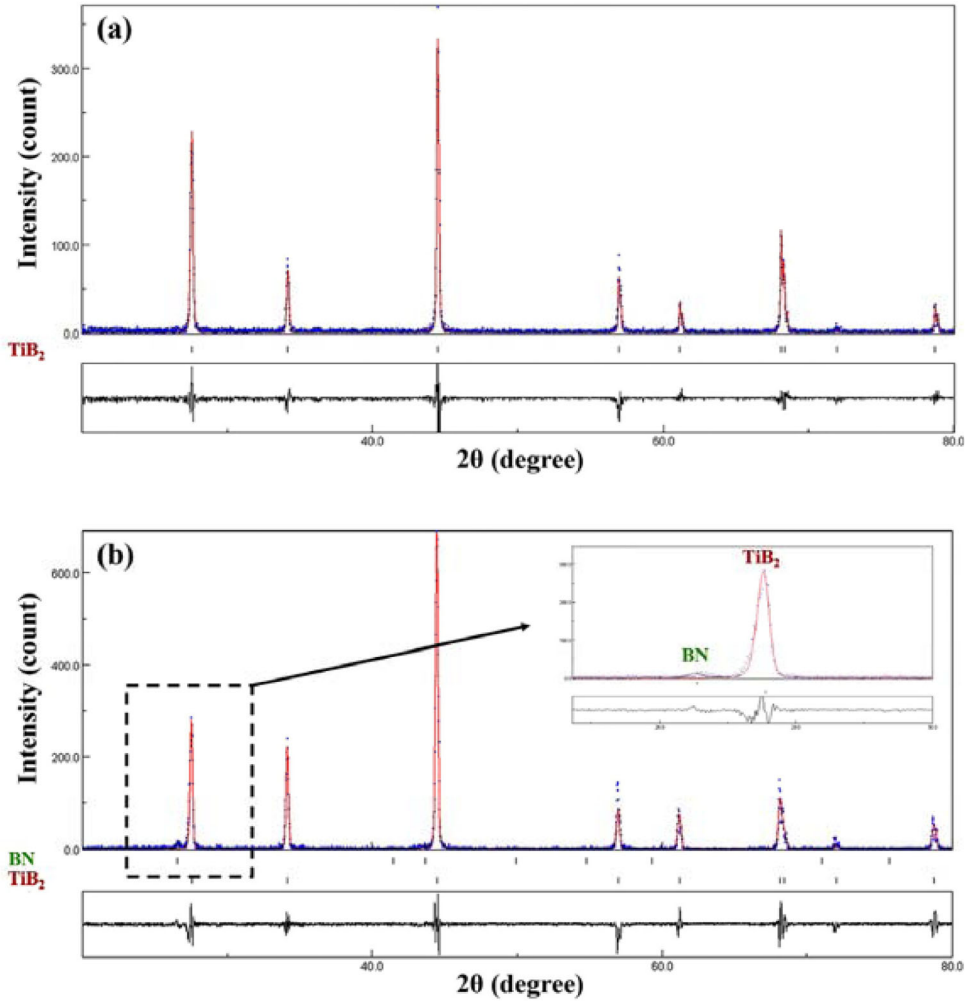

Fig. 2. XRD patterns after Rietveld refinement: (a) TiB_2 (reprinted with permission from Ref. 41), and (b) TC sample (reprinted with permission from Ref. 42).

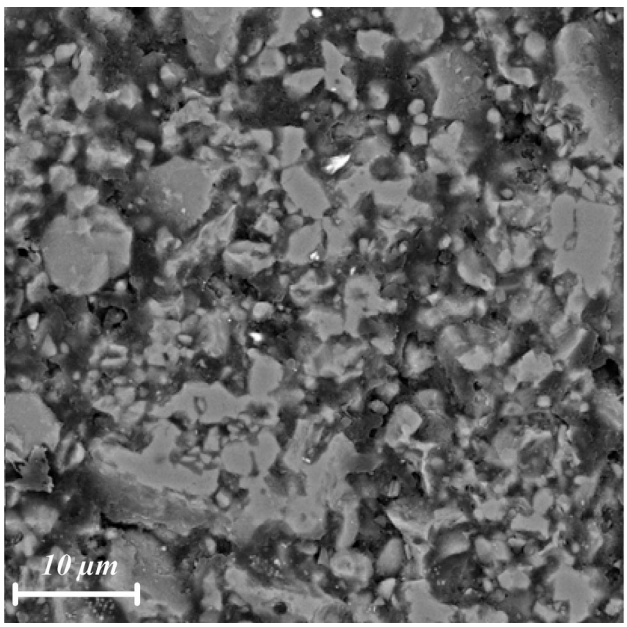

Fig. 3. FESEM micrographs of TC composite.

in this composite.[45] In contrast to the voids and porosity that are usually observable in the composite, the worn surface exhibits no detectable porosity or gaps. Most of the micro-cracks resulting from cyclic loading have been filled during the wear process of carbon-rich zones, matrix phase, and tungsten pin debris.

Three distinct points on the wear surface were selected for elemental analysis using energy-dispersive X-ray spectroscopy (EDS). Figure 7 displays the analyzed points and their corresponding elemental composition results. Point “a” exhibits a distinct aggregation of boron (B) and titanium (Ti), corresponding to the matrix phase (TiB_2). The trace carbon (C) detected at this location originates from an ultra-thin tribofilm formed through wear-induced exfoliation of carbon-rich zones. In Point “b”, analyzed within a dark region, carbon concentration surpasses both titanium and boron. Tungsten (W) particles are also identified, confirming the filling of voids. Point “c” reveals additional oxygen (O) signatures, indicative of oxide impurities on the

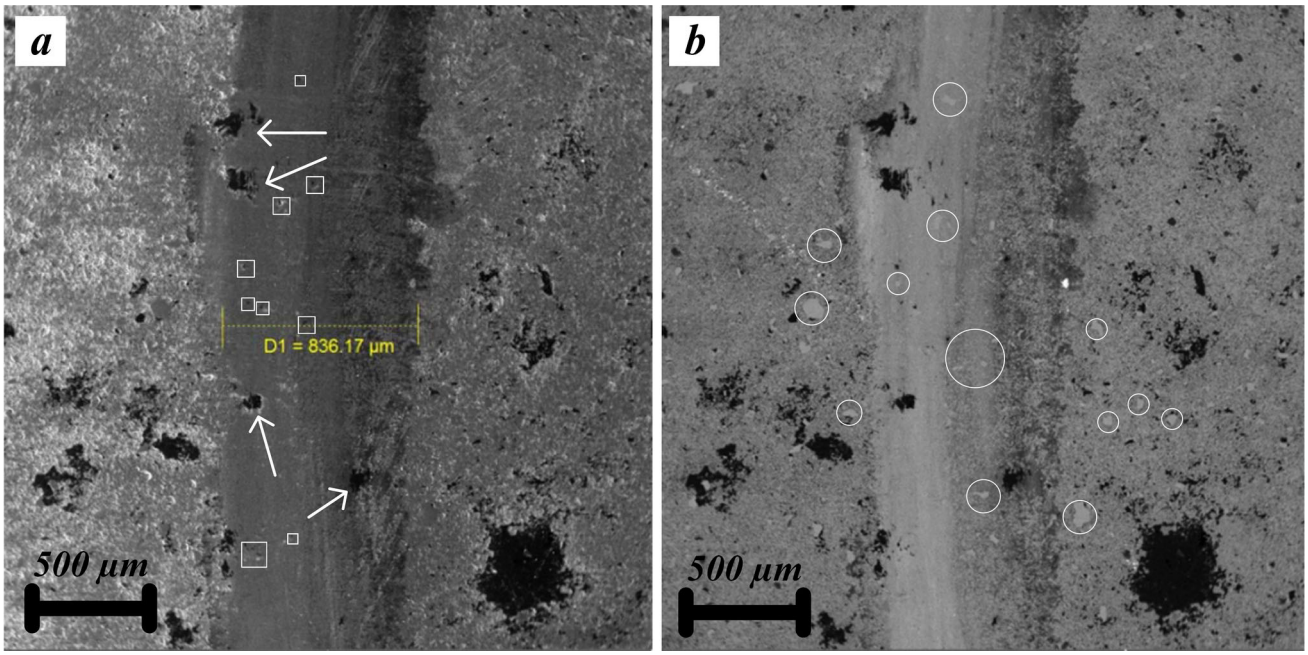

Fig. 4. FE-SEM images of the worn surface of TC composite, (a) secondary electron mode, (b) backscattered electron mode.

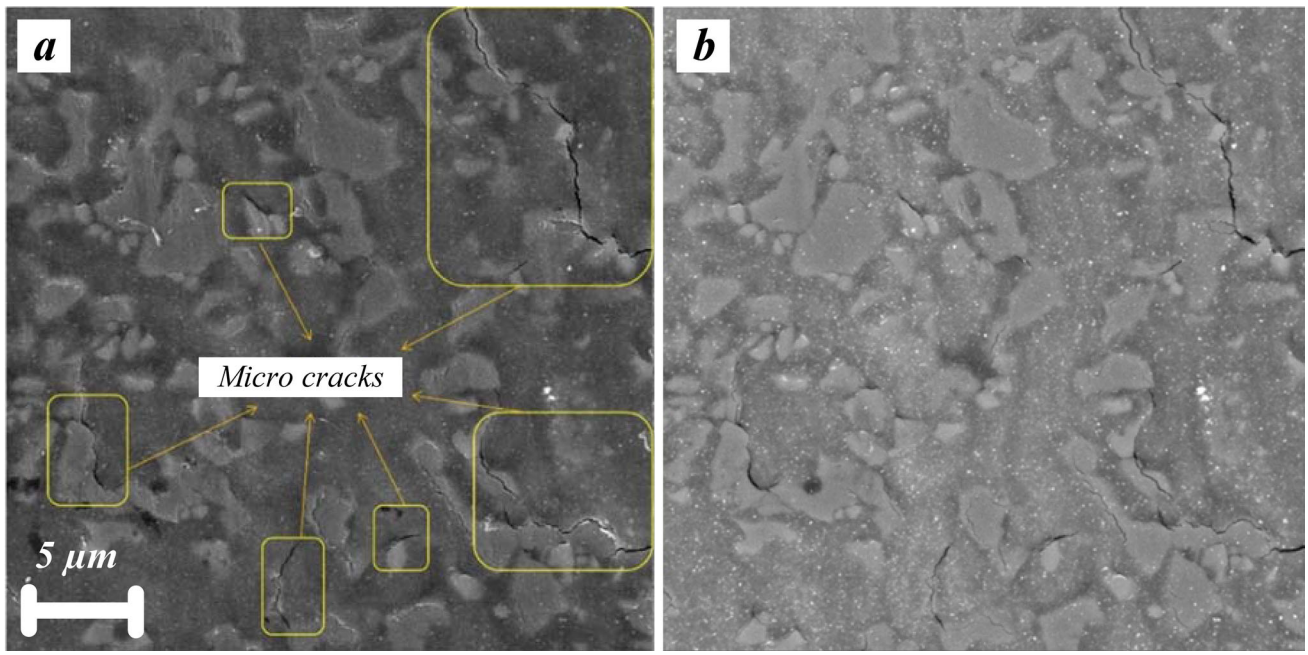

Fig. 5. Higher magnification FESEM images of the worn surface of TC composite: (a) secondary electron image, (b) backscattered electron image.

wear surface. Since direct hardness measurement of the surface was not feasible because of very high hardness of composite, the hardness was estimated using wear data and Archard's formula (Eq. 3), where k is a dimensionless constant that represents the wear resistance of the material (a higher k value indicates more severe wear), N is the normal load (N), S is total sliding distance (m), and H is the hardness (Pa). The k is set to 10^{-2} for the composite against the WC pin during the dry pin on disk wear test:

$$\text{Archard's wear} = k\frac{S \times N}{H} \tag{3}$$

The estimated hardness was about 41.2 GPa. The hardness for different TiB_2-based composites has been reported from around 25 GPa[38] to about

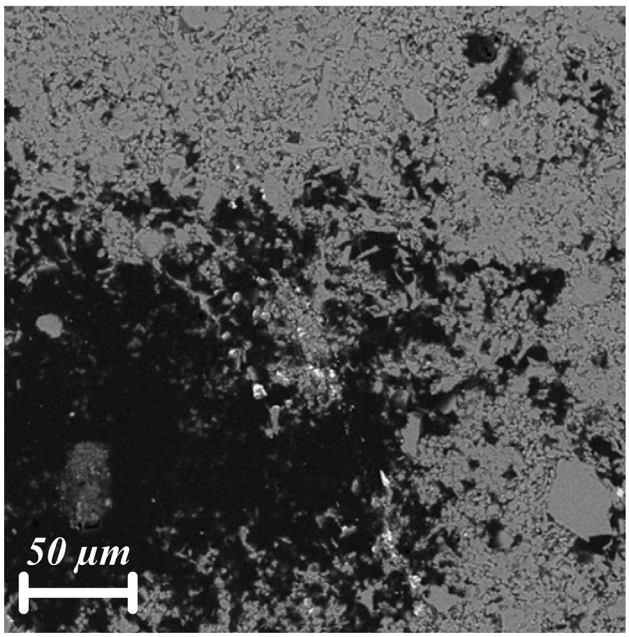

Fig. 6. Carbon-rich area on the worn surface of the composite (reprinted from Ref. 46, under the terms of the Creative Commons CC BY license).

32 GPa.[47] The exceptionally high hardness of the present composite can be attributed to the presence of in situ formed hard phases.

Figure 8 reveals the coefficient of friction (COF) of the composite concerning the sliding distance. The average coefficient of friction was measured at approximately 0.67, which is higher than that of monolithic TiB_2 ($\sim$ 0.45).[38] This indicates that the tribofilm formed in this composite does not reduce the friction coefficient as effectively as some other additives, such as SiC. The plot also exhibits fluctuations, with the COF increasing from 0.5 at the initial stage of wear to about 0.8 by the end of the sliding distance. In the first 20 m, the COF rises significantly before stabilizing.

The friction coefficient starts low due to poor contact and contamination but increases as surfaces adapt, tribofilms form, and true contact improves. Eventually, it stabilizes when equilibrium is reached between wear and surface modification.

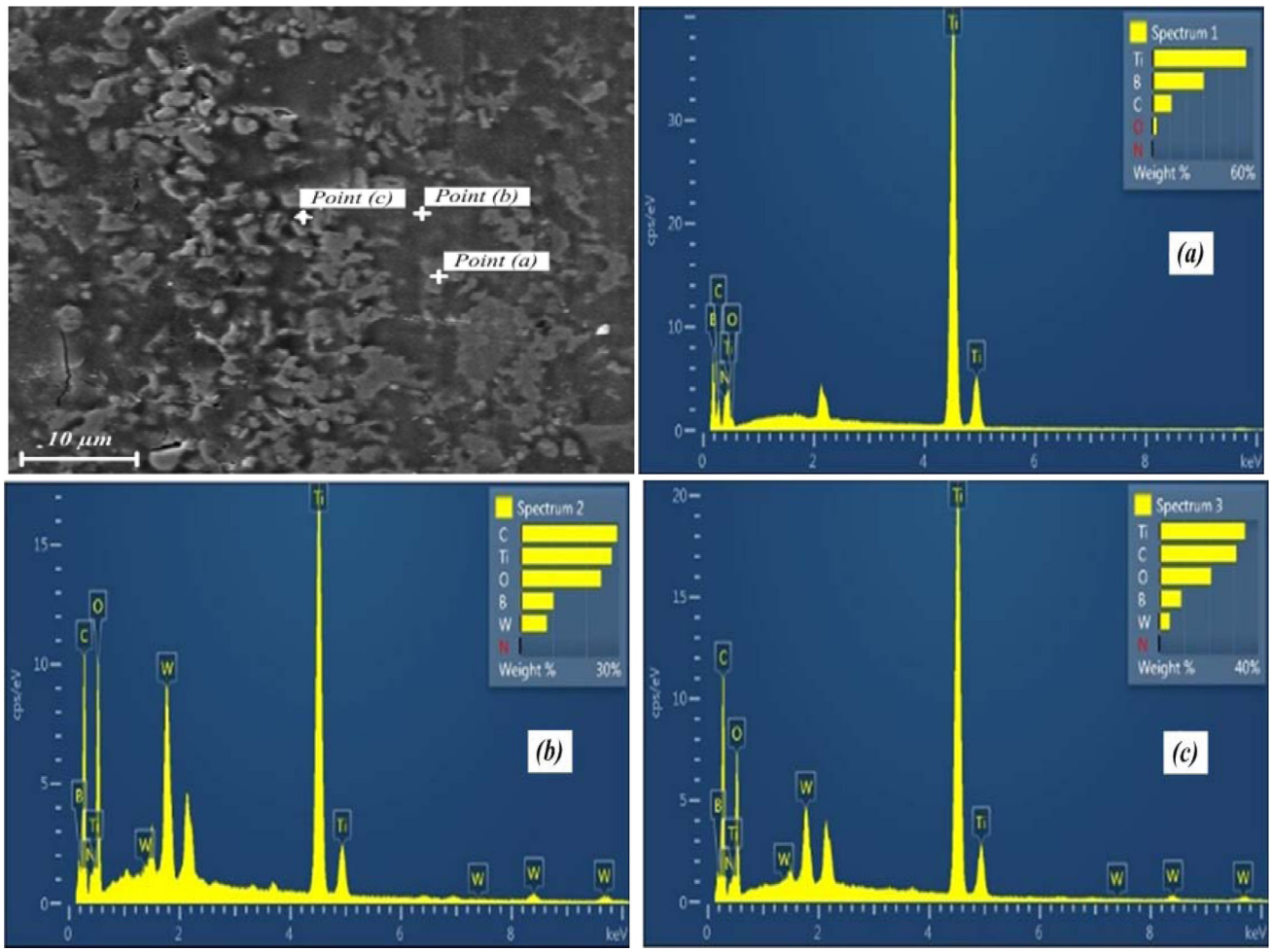

Fig. 7. The EDS analysis of the worn surface.

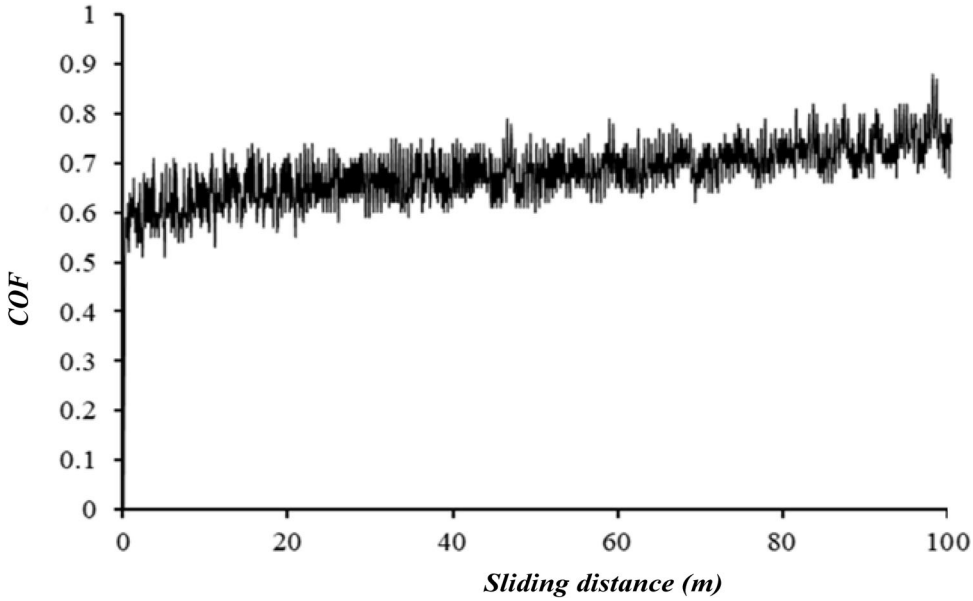

Fig. 8. Coefficient of friction of the composite concerning the sliding distance.

CONCLUSION

This study has successfully demonstrated the efficacy of g-C_3N_4 as a sintering aid and reinforcing phase in TiB_2 composites, processed via SPS at 1900°C. The resulting TiB_2-10 wt% g-C_3N_4 composite achieved densification (91.3% relative density) and exhibited a 50% reduction in wear rate (2.455×10^{-4} mm^3/N m) compared to monolithic TiB_2, alongside an ultrahigh estimated hardness of 41.2 GPa. Microstructural and tribological analyses revealed that the improved wear resistance stemmed from:

- Probably in situ formation of B_4C and BN hard allotropes, enhancing hardness and fracture toughness.
- Carbon-rich tribofilms and hexagonal BN particles, filling surface grooves and mitigating abrasive wear.
- Reduced porosity minimizes the stress concentration and crack propagation.

However, the composite's higher coefficient of friction (0.67) suggests that, while g-C_3N_4 improves wear resistance, its tribofilm provides less effective lubrication than additives like SiC. These results position g-C_3N_4 as a viable, cost-effective reinforcement for TiB_2 in extreme wear applications, advancing the development of next-generation UHTC composites.

FUNDING

Open access funding provided by the Scientific and Technological Research Council of Türkiye (TÜBİTAK). This research work was financially supported by Synsint Research Group (Grant No. SS-2026-003).

CONFLICT OF INTEREST

The authors have no relevant financial or non-financial interests to disclose.

OPEN ACCESS

REFERENCES

1. B.C. Wyatt, S.K. Nemani, G.E. Hilmas, E.J. Opila, and B. Anasori, *Nat. Rev. Mater.* 9, 773 (2023).
2. M. Shojaie-Bahaabad, M. Bozorg, M. Najafizadeh, and P. Cavaliere, *Ceram. Int.* 50, 9937 (2024).
3. L. Zoli, F. Servadei, G. Bassi, A. Rossi, M. Montesi, A. Vinci, D. Sciti, and S. Panseri, *J. Eur. Ceram. Soc.* 44, 729 (2024).

4. E. Wuchina, E. Opila, M. Opeka, B. Fahrenholtz, and I. Talmy, *Electrochem. Soc. Interface* 16, 30 (2007).
5. J. Binner, M. Porter, B. Baker, J. Zou, V. Venkatachalam, V.R. Diaz, A. D'Angio, P. Ramanujam, T. Zhang, and T.S.R.C. Murthy, *Int. Mater. Rev.* 65, 389 (2020).
6. K. Cui, H. Mao, Y. Zhang, J. Wang, H. Wang, T. Tan, and T. Fu, *Compos. Interfaces* 29, 729 (2022).
7. F.-Z. Dai, B. Wen, Y. Sun, Y. Ren, H. Xiang, and Y. Zhou, *J. Mater. Sci. Technol.* 123, 26 (2022).
8. H. Zhang, D.D. Jayaseelan, I. Bogomol, M.J. Reece, C. Hu, S. Grasso, and W.E. Lee, *J. Alloys Compd.* 785, 958 (2019).
9. Z. Peng, W. Chenchen, Z. Shengfeng, G. Baisong, Z. Zhiguo, Y. Zhentao, and L. Wei, *Powder Metall. Met. Ceram.* 61, 560 (2023).
10. J. Gu, J. Zou, J. Liu, H. Wang, J. Zhang, W. Wang, and Z. Fu, *J. Eur. Ceram. Soc.* 40, 1086 (2020).
11. A.S. Mukasyan, and A.S. Rogachev, *Int. J. Appl. Ceram. Technol.* 22, e70044 (2025).
12. Z. Cao, J. Sun, K. Zhang, W. Ji, K. Cai, B. Li, B. Liu, and C. Fan, *Compos. Part A Appl. Sci. Manuf.* 185, 108318 (2024).
13. E. De Bona, C. Manière, V.M. Sglavo, and M. Biesuz, *J. Eur. Ceram. Soc.* 44, 567 (2024).
14. W. Sun, Y. Tian, S. Xu, L. Liu, and Y. Lu, *Int. J. Appl. Ceram. Technol.* 21, 195 (2024).
15. T.O. Prikhna, A.S. Lokatkina, P.P. Barvitskyi, M.V. Karpets, S.S. Ponomaryov, A.A. Bondar, B. Büchner, J. Werner, R. Kluge, V.E. Moshchil, O.I. Borymskyi, L.M. Devin, S.V. Rychev, R. Haber, Z.A. Yasar, B. Matovic, M. Rucki, and O.V. Prisyazhna, *J. Superhard Mater.* 45, 321 (2023).
16. B.R. Golla, A. Mukhopadhyay, B. Basu, and S.K. Thimmappa, *Prog. Mater. Sci.* 111, 100651 (2020).
17. R.G. Munro, *J. Res. Natl. Inst. Stand. Technol.* 105, 709 (2000).
18. B. Basu, G.B. Raju, and A.K. Suri, *Int. Mater. Rev.* 51, 352 (2006).
19. R. Telle, and G. Petzow, *Mater. Sci. Eng. A* 105–106, 97 (1988).
20. A. Turan, M. Bugdayci, and O. Yucel, *High Temp. Mater. Process.* 34, 185 (2015).
21. G.B. Raju, and B. Basu, *J. Am. Ceram. Soc.* 90, 3415 (2007).
22. Y. Zheng, J. Zou, W. Liu, W. Wang, W. Ji, and Z. Fu, *J. Eur. Ceram. Soc.* 43, 5117 (2023).
23. C. Öztürk, and G. Can, *J. Dent. Res. Dent. Clin. Dent. Prospects* 13, 247 (2019).
24. N. Juntavee, and S. Attashu, *J Clin Exp Dent* 10, e794 (2018).
25. N.S. Peighambardoust, Ç. Çevik, T. Assar, S. Jung, S.Y. Lee, and J.H. Cha, *Synth. Sinter.* 1, 28 (2021).
26. M. Sakkaki, and S.M. Arab, *Synth. Sinter.* 2, 176 (2022).
27. Z. Ahmadi, M. Zakeri, A. Habibi-Yangjeh, and M. Shahedi Asl, *Ceram. Int.* 45, 21512 (2019).
28. L. Zhang, H. Qi, G. Li, D. Wang, T. Wang, Q. Wang, and G. Zhang, *Mater. Des.* 129, 192 (2017).
29. V. Matějka, M. Leonardi, P. Praus, G. Straffelini, and S. Gialanella, *Metals (Basel)* 12, 123 (2022).
30. S.D. Oguntuyi, O.T. Johnson, and M.B. Shongwe, *Met. Mater. Int.* 27, 2146 (2021).
31. M. Shahedi Asl, Z. Ahmadi, S. Parvizi, Z. Balak, and I. Farahbakhsh, *Ceram. Int.* 43, 13924 (2017).
32. M. Sajdak, K. Kornaus, D. Zientara, N. Moskała, S. Komarek, K. Momot, E. Golis, Ł Zych, and A. Gubernat, *Crystals* 14, 212 (2024).
33. Z.-Y. Hu, Z.-H. Zhang, X.-W. Cheng, F.-C. Wang, Y.-F. Zhang, and S.-L. Li, *Mater. Des.* 191, 108662 (2020).
34. X. Wei, C. Back, O. Izhvanov, C. Haines, and E. Olevsky, *Materials (Basel).* 9, 577 (2016).
35. S. Mohammad Bagheri, M. Vajdi, F. Sadegh Moghanlou, M. Sakkaki, M. Mohammadi, M. Shokouhimehr, and M. Shahedi Asl, *Ceram. Int.* 46, 7615 (2020).
36. E. Ranjbarpour Niari, M. Vajdi, M. Sakkaki, S. Azizi, F. Sadegh Moghanlou, and M. Shahedi Asl, *Int. J. Appl. Ceram. Technol.* 19, 344 (2022).
37. B. Ramesh, E. Showman, S.A.M. Abraar, K.K. Saxena, M.Y. Tharwan, N. Alsaadi, S. Al Sofyani, and A.H. Elsheikh, *Materials* 15, 7096 (2022).
38. S.D. Oguntuyi, M.B. Shongwe, L. Tshabalala, O.T. Johnson, and N. Malatji, *Arab. J. Sci. Eng.* 48, 2889 (2023).
39. A. Kovalčíková, P. Tatarko, R. Sedlák, D. Medveď, Z. Chlup, E. Múdra, and J. Dusza, *J. Eur. Ceram. Soc.* 40, 4860 (2020).
40. A. Dasari, Z.-Z. Yu, and Y.-W. Mai, *Mater. Sci. Eng. R. Rep.* 63, 31 (2009).
41. Z. Hamidzadeh Mahaseni, M. Dashti Germi, Z. Ahmadi, and M. Shahedi Asl, *Ceram. Int.* 44, 13367 (2018).
42. M. Sakkaki, Z. Ahmadi, S.M. Arab, M. Farvizi, and M. Shahedi Asl, *JOM* 76, 6207 (2024).
43. R. Liu, and D. Li, *Wear* 251, 956 (2001).
44. M. Terheci, *Mater Charact* 45, 1 (2000).
45. A. Twardowska, and M. Kowalski, *Materials* 17, 2379 (2024).
46. M. Sakkaki, and S.M. Arab, *Synth. Sinter.* 3, 73 (2023).
47. S.D. Oguntuyi, N. Malatji, M.B. Shongwe, O.T. Johnson, C. Khoathane, and L. Tshabalala, *Int. J. Light. Mater. Manuf.* 5, 326 (2022).